nature photonics

Article

https://doi.org/10.1038/s41566-024-01486-z

Chirality conferral enables the observation of hyper-Raman optical activity

Received: 12 October 2023

Accepted: 25 June 2024

Published online: 31 July 2024

Check for updates

Robin R. Jones[1,2], John F. Kerr[1,2], Hyunah Kwon[3,4], Samuel R. Clowes[5], Ruidong Ji[1,2], Emilija Petronijevic[6], Liwu Zhang[7], G. Dan Pantoș[5], Brian Smith[8], Tim Batten[8], Peer Fischer[3,4], Daniel Wolverson[1,2], David L. Andrews[9] & Ventsislav K. Valev[1,2]

Chirality conferral is fundamental for understanding the origin of life, and it is of direct importance for synthesizing new pharmaceuticals in the face of growing antibiotic resistance. Human-made, self-assembling nanostructures replicate the biological chirality conferral processes utilizing covalent and non-covalent bonds. However, chirality conferral from one form of matter to another via electromagnetic fields is more subtle and less explored. Here we report chirality conferral between gold nanohelices and achiral molecules (crystal violet). This conferral enables the experimental observation of a physical effect predicted in 1979—hyper-Raman optical activity. To benefit from Fermi's golden rule, the chirality conferral system was designed as doubly resonant, with the nanohelices and molecules resonating at the fundamental frequency and at the second-harmonic, respectively. We provide a theoretical framework for our results that expands the original mathematical formalism to include surface-enhanced hyper-Raman scattering and the chirality conferral process. Our results demonstrate that field-driven chirality conferral mechanisms are opening up entire fields of research, as exemplified by the discovery of a physical phenomenon.

In life as in human-made self-assembly processes, chirality is conferred between building blocks and across hierarchically organized assemblies with emerging and increasing complexity[1–3]. Chirality conferral can occur, for instance, within chemical reactions[4], from chiral molecules to achiral inorganic materials, or from chiral inorganics to achiral molecules[5–9]. Molecular chirality has been conferred to achiral plasmonic silver nanoparticles[10], gold nanorods[11], gold nanoparticles[12] and solid-state lattices in organic–inorganic perovskites[13,14]. Conversely, the chirality of chiral nanotubes has been conferred to organic molecules[15]. The chirality conferral process is not trivial[16], and it should be noted that some achiral molecules that adsorb on inorganic surfaces can become chiral or form chiral organic–inorganic entities[17,18]. Chirality can also be conferred from the macroscale to the nanoscale, for example via macroscale twist of a material that contains plasmonic nanoparticles[19]. Several previous works, including work from some of the co-authors here, have focused on the chirality conferral from plasmonic nanoparticles to achiral molecules, but crucially, they have not established the dependence on intrinsic chirality by showing rotation invariance of the results[20–22]. Moreover, while previous studies have explored photon-to-matter chirality transfer[23], chirality conferral from the electromagnetic field of nanoparticles to molecules has hardly been explored.

[1]Centre for Photonics and Photonic Materials, Department of Physics, University of Bath, Bath, UK. [2]Centre for Nanoscience and Nanotechnology, Department of Physics, University of Bath, Bath, UK. [3]Max Planck Institute for Medical Research, Heidelberg, Germany. [4]Institute for Molecular Systems Engineering and Advanced Materials, Heidelberg University, Heidelberg, Germany. [5]Department of Chemistry, University of Bath, Bath, UK. [6]SBAI Department, La Sapienza University of Rome, Rome, Italy. [7]Department of Environmental Science and Engineering, Fudan University, Shanghai, China. [8]Renishaw plc, New Mills, Kingswood, UK. [9]School of Chemistry, University of East Anglia, Norwich, UK. e-mail: v.k.valev@bath.ac.uk

https://doi.org/10.1038/s41566-024-01486-z

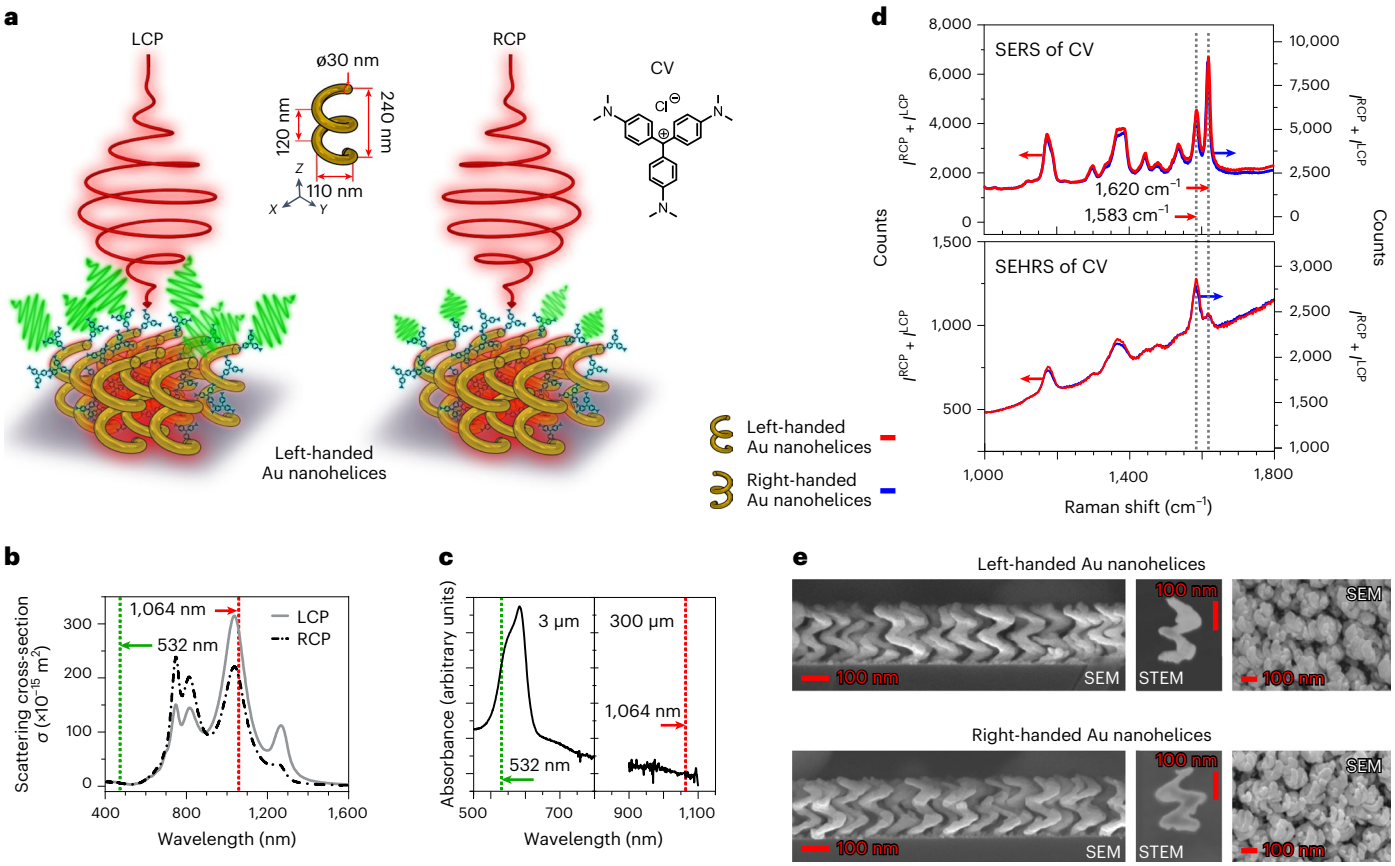

Fig. 1 | CV molecules on Au nanohelices constitute a doubly resonant system for hyper-Raman scattering. a, Schematic diagram of the reported hyper-Raman optical activity effect: illumination with LCP and RCP results in different intensities of hyper-Raman scattering. **b**, The nanohelices have strong resonances at 1,064 nm and not at 532 nm, as demonstrated by simulations of the Rayleigh scattering cross-section spectra. **c**, The crystal violet (CV) molecules have strong resonances at 532 nm and not at 1,064 nm, as shown by their absorbance spectra. **d**, Surface-enhanced Raman scattering (SERS) (top) and surface-enhanced hyper-Raman scattering (SEHRS) (bottom) circular intensity sum (CIS) spectra of CV. **e**, Scanning electron microscopy (SEM) and scanning electron transmission microscopy (STEM) images of Au nanohelices. Left: SEM images present left- and right-handed nanohelix arrays on Si wafer. Middle: STEM images present a single nanohelix isolated and deposited on a STEM grid. Right: SEM images present top-down views of left-handed (left) and right-handed (right) Au nanohelices.

Here, we unambiguously demonstrate chirality conferral from the electromagnetic field of chiral plasmonic nanoparticles (Au nanohelices) to crystal violet (CV) molecules that are achiral (on average, as we explain below). This conferral results in the discovery of a new chiral optical effect—hyper-Raman optical activity—that was predicted 45 years ago by one of the co-authors (et al.)[24]. Previous attempts to demonstrate this phenomenon have been reported unsuccessful, due to polarization artefacts and due to thermal effects associated with high-power laser illumination[25]. We recorded that, upon illumination at 1,064 nm, there is a difference of hyper-Raman spectra (that is, those around 532 nm) for right- and left-handed circularly polarized light (RCP and LCP, respectively), known as the circular intensity difference (CID)[26]. The CID spectrum from the achiral CV changes sign, depending on the handedness of the nanohelices. Importantly, we demonstrate that our data correspond to intrinsic chirality[27]. The arrays of nanohelices exhibit extrinsic chirality in linear reflection, in second-harmonic generation circular dichroism (CD)[28] and in second-harmonic generation optical rotation[29]. The extrinsic chirality results in a sign change of the 'chiroptical' response upon rotating the sample; such sample rotation effects have also been shown to affect Raman scattering[30]. By contrast, sample rotation that does not affect the Raman spectra is associated with antisymmetric Raman tensors, which Barron introduced to explain true Raman optical activity[31–33]. We demonstrate that the sign of the Raman and hyper-Raman peaks in our CID spectra does not depend on sample rotation, which is an unambiguous signature of chirality. We also show that no hyper-Raman optical activity is observed from achiral gold nanostructures coated with CV, thereby confirming the role of the nanohelices' geometry. While in our observation we make use of chirality conferral by plasmonic nanohelices to achiral molecules, the original paper on hyper-Raman optical activity focused on chiral molecules alone. To take this difference into account, here we expand the original theory to surface-enhanced hyper-Raman scattering (SEHRS) and we include the chirality conferral mechanism. We present the leading light–matter interaction processes and their quantum amplitudes, whose modulus square yields the measured hyper-Raman signal intensity. We show how the chiroptical response emerges from the sum of electric dipole quantum amplitude contributions and terms that include contributions from magnetic dipoles or electric quadrupoles. Our work demonstrates that chirality conferral can lead to new physics, as illustrated by the observation of a new phenomenon.

Figure 1a shows a diagram of our experiment, where LCP and RCP are incident on an array of left-handed plasmonic nanohelices, made of gold. The dimensions of the helices and the chemical formula for CV are shown in inset. As can be seen, the CV molecule's formula is achiral; however, it is energetically unfavourable for the three branches to remain coplanar. Due to steric hindrance, the molecule exhibits rotational flexibility, with the branches rotating to adopt left-handed and right-handed orientations, in an overall propeller-like configuration. Each molecule can transition between these configurations. Therefore, the molecule is achiral because of its dynamic behaviour, which

https://doi.org/10.1038/s41566-024-01486-z

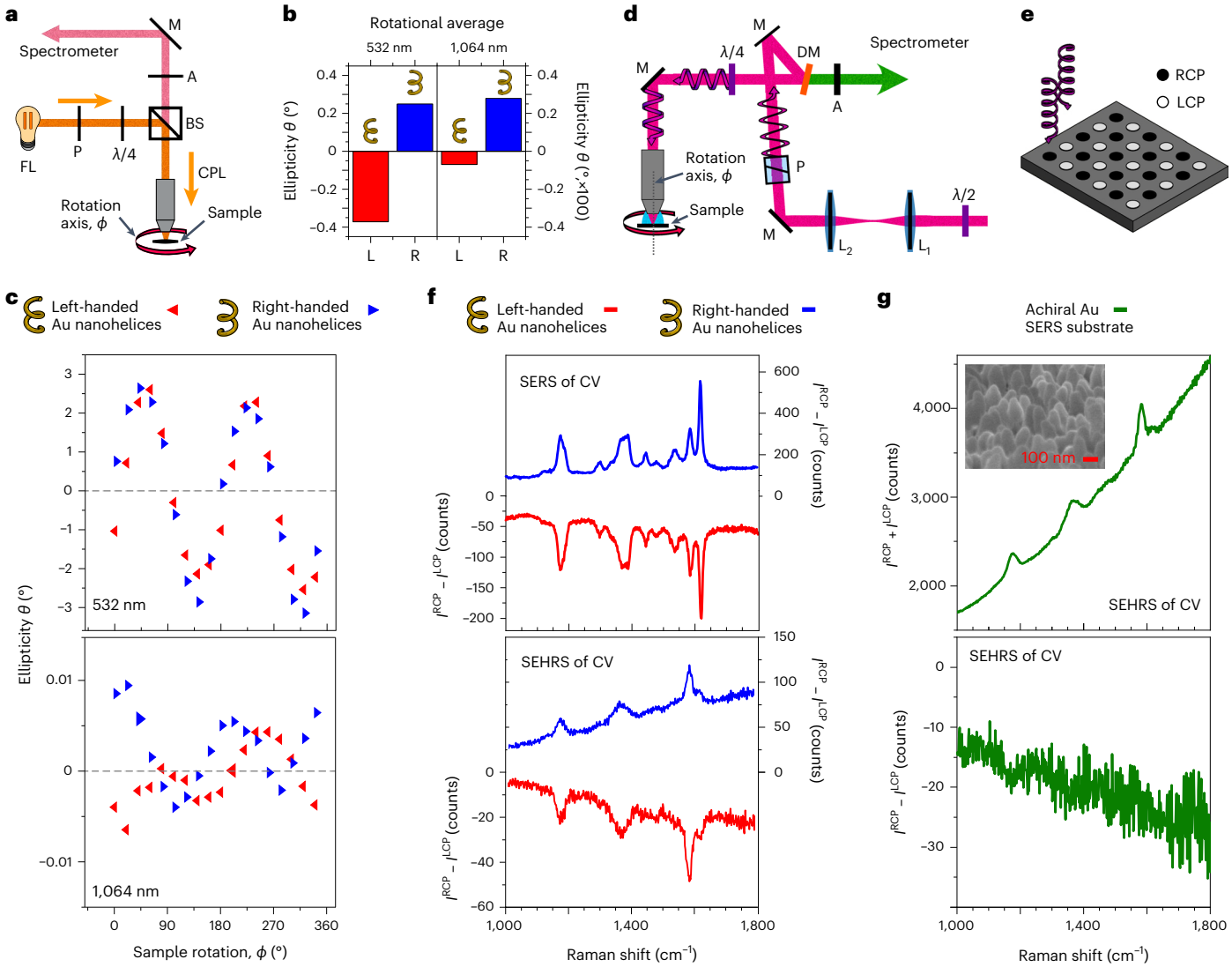

Fig. 2 | Extrinsic chirality that is clearly present in reflectivity measurements with circularly polarized light does not seem to affect the rotationally averaged Raman spectra. a, Diagram of the reflective microscope setup (FL, filament lamp; P, polarizer; λ/4, quarter-waveplate; CPL, circularly polarized light; BS, beam splitter; A, analysing polarizer (analyser); M, mirror). **b**, Rotationally averaged ellipticity from reflection spectroscopy are not mirror images for the two enantiomorphs. **c**, Reflection ellipticity versus sample angle (rotation) at 532 nm and 1,064 nm reveal extrinsic chirality—the ellipticity depends strongly on the sample rotation and changes sign several times. **d**, Diagram of the hyper-Raman instrument (λ/2, half-waveplate; L1 and L2, collimation lenses; M, mirror; P, polarizer; DM, dichroic mirror; λ/4, quarter-waveplate; A, analysing polarizer (analyser)). **e**, Illustration of the mapping technique used—illumination was performed in 5-by-6 arrays, with alternating right- and left-handed circularly polarized light (RCP and LCP, respectively) illumination for each spot. **f**, The difference of SERS and SEHRS spectra, acquired for RCP and LCP illumination, from CV molecules deposited on left- and right-handed Au nanohelices. **g**, The sum and difference of hyper-Raman spectra acquired for RCP (top) and LCP (bottom) illumination, from CV molecules on commercial achiral SERS substrates. The inset shows an SEM image of the sample surface.

allows a continuous conversion between the left- and right-handed configurations, at room temperature. Strictly speaking, a CV molecule is achiral 'on average'. With many molecules, at any moment in time, there is a racemic mixture of left- and right-handed configurations. Depending on the handedness of circularly polarized light, the intensity of the Raman scattered light from CV changes. The nanohelices were designed to exhibit a peak in their scattering cross-section at the fundamental frequency of laser illumination (1,064 nm) but not at the second-harmonic frequency (532 nm), as it is shown in Fig. 1b and Supplementary Fig. 1. Details of the simulation parameters are provided in Methods. Conversely, the CV molecules lack resonances at 1,064 nm but exhibit pronounced energy states around 532 nm, as can be seen in Fig. 1c. This combined system is therefore doubly resonant, which favours the expression of hyper-Raman scattering, by Fermi's golden rule.

The surface-enhanced Raman scattering (SERS) and SEHRS spectra of the CV can be obtained by summing the spectra recorded for LCP and RCP illumination, on both left- and right-handed nanohelices, as shown in Fig. 1d. All the Raman spectra were acquired with a Raman spectrometer (InVia, Renishaw), and the CV spectra are in agreement with previous reports[34]. An important feature of the plasmonic nanohelices is that they are oriented—all are facing the same direction, as demonstrated by the scanning electron microscopy (SEM) and scanning transmission electron microscopy (STEM) images in Fig. 1e. This orientation suggests that strong extrinsic chirality is present in the system.

In chiroptical studies, it is important to distinguish intrinsic/true from extrinsic chirality, anisotropy effects on the polarization and artefacts[35]. In the case of ordered materials, such as our metal nanostructures, the ordering itself can produce chirality-like effects—a behaviour that has been referred to as 'pseudo chirality'[36] or 'extrinsic

https://doi.org/10.1038/s41566-024-01486-z

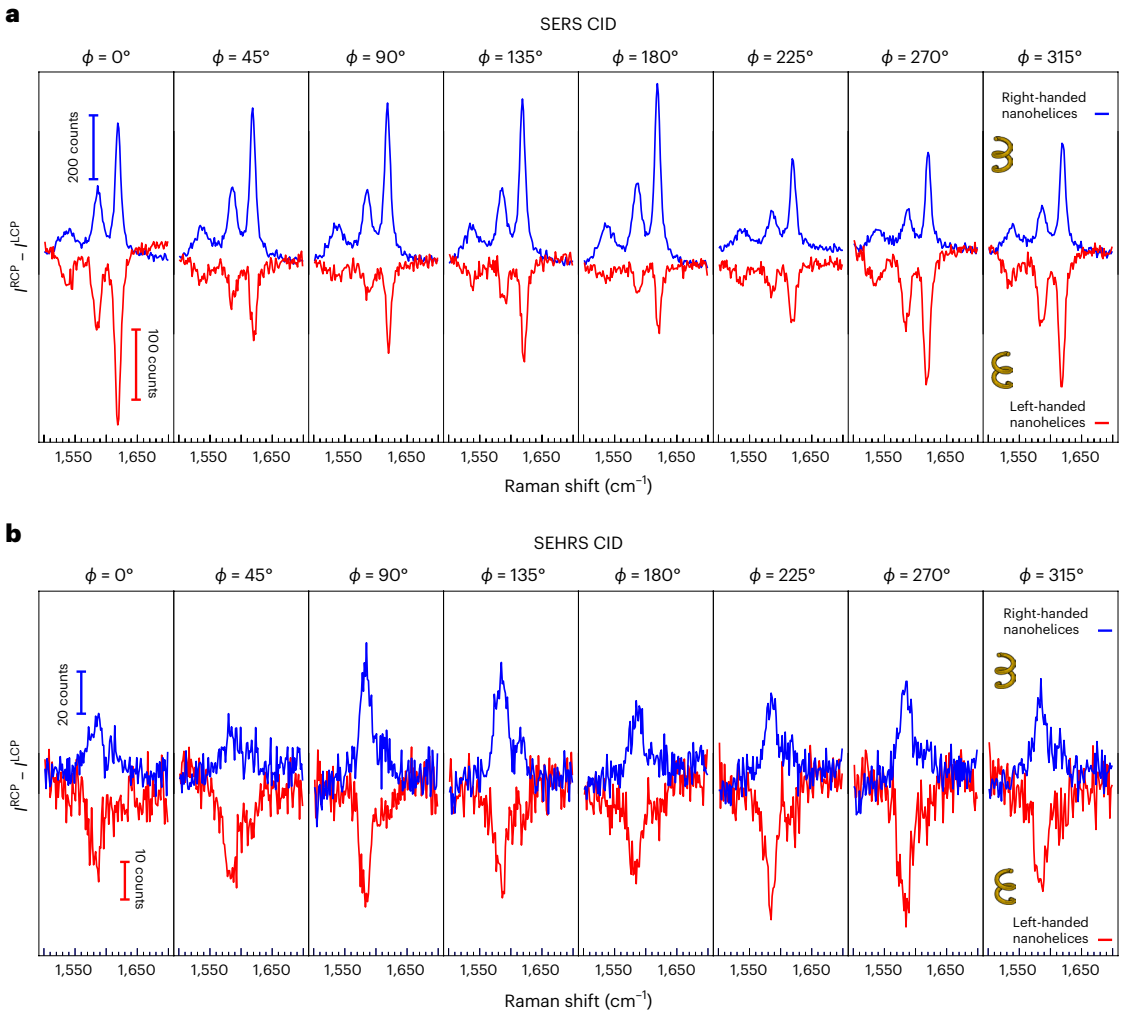

Fig. 3 | The sign of the Raman spectra does not change upon sample rotation, which indicates that the effect originates from intrinsic chirality. a,**b**, The SERS (**a**) and SEHRS (**b**) CID spectra are plotted for eight different samples rotation angles. The CID spectra are consistently negative for CV on left-handed nanohelices (in red) and positive for CV on right-handed nanohelices (in blue).

chirality'[37]. To address this question, we characterized the reflectance of our samples, using the setup described in Fig. 2a. For each of them, we calculated the ellipticity (θ), defined by

$$\theta = \frac{180}{\pi}\tan^{-1}\left[\left(\sqrt{I^{RCP}} - \sqrt{I^{LCP}}\right) \Big/ \left(\sqrt{I^{RCP}} + \sqrt{I^{LCP}}\right)\right], \qquad (1)$$

where I^{RCP} and I^{LCP} represent the intensities of detected light for RCP and LCP illumination, respectively. Figure 2b shows the rotationally averaged ellipticity at 532 nm and 1,064 nm, respectively. The data were extracted from the CD spectra shown in Supplementary Fig. 2. We note that at 532 nm and at 1,064 nm the sign of the ellipticity is opposite for left- and right-handed helices. Although for left- and right-handed nanohelices, the ellipticity plots in Supplementary Fig. 2 are close to mirror images, at each wavelength, a very strong sample rotation dependence can be observed, as seen in Fig. 2c. Figure 2c shows the ellipticity as a function of sample rotation for 532 nm and for 1,064 nm. The plots were obtained from averaging 11 curves in the 528–536 nm range and in the 1,056–1,072 nm range, respectively. We note that there is little spectral variation across these ranges and that the Ti:Sapphire pulse used in the hyper-Raman experiments at 1,064 nm is about 15 nm in width. For all curves in Fig. 2c, the ellipticity changes sign four times upon sample rotation. Because chirality is invariant upon rotation, this ellipticity cannot be measuring chirality alone. There are several physical mechanisms that affect these measurements.

These nanohelices are arranged in arrays that exhibit a local hexagonal lattice. Because of the way they are fabricated (that is, all at once), the nanohelices are oriented in the same way, with terminations pointing towards the source of deposition. Thus, the samples also exhibit unidirectional anisotropy. Moreover, it is possible that the nanohelices are locally slightly tilted, with their main axis deviating from the z axis, which could be another source of unidirectional anisotropy. When illuminated, electromagnetic resonances are excited both within each helix and between helices, depending on the wavelength of illumination. The intrinsic chirality of the helices plays a role, but the extrinsic chirality due to unidirectional anisotropy is a strongly competing effect. Additionally, because we use achromatic waveplates, the retardation is not identical across the full spectrum of operation—there is a slight linearly polarized component and it depends on wavelength. At each wavelength, for LCP and RCP positions of the waveplate, the linearly polarized components are at 90° to each other. Therefore, rotating the sample for LCP and RCP illumination affects several wavelength-dependent mechanisms. Distinguishing and optimizing these individual mechanisms is very important for the field of metasurfaces—for instance, to produce ultrathin polarizers for circularly polarized light (CPL). In the present context, the key point is that the ellipticity is observed to change sign several times, as the sample rotates. It is clear that, in these reflection experiments, polarization imperfection (also identified as a problem

in previous attempts to observe hyper-Raman optical activity)[25] and material anisotropy are present. But would they affect the (hyper-) Raman scattering of CV?

The diagram of the Raman and hyper-Raman scattering setup can be seen in Fig. 2d. Circularly polarized light was obtained with the help of a polarizer and a quarter-wave plate ($\lambda/4$). Possible contributions from experimental artefacts, such as light circularity (Supplementary Fig. 3), quenching or photodecomposition of CV, variations in the number of illuminated molecules and so on, have been addressed (Supplementary Information).

In Fig. 2e, the rotationally averaged SERS and SEHRS spectra were obtained from averaging a total of 360 RCP (I^{RCP}) and 360 LCP (I^{LCP}) spectra. Within each sample, the plotted CID ($I^{RCP} - I^{LCP}$) is therefore free from artefacts related to the number of molecules or quenching. Because the left- and right-handed nanohelices are grown separately, there are geometrical (batch) difference between them. Moreover, the left- and right-handed nanohelices were spin-coated with CV separately; hence, a difference in molecular concentration exists. Accordingly, the amplitude of the CID peaks in Fig. 2f differs between left- and right-handed nanohelices. However, the sign of all the peaks is opposite, for both SERS and SEHRS, which is an indication of the hyper-Raman optical activity effect.

To confirm the role of the nanohelices, we repeated our experiments using achiral nanostructures from a commercial (Silmeco), SERS substrate, made of Au. An SEM image of the substrate surface is displayed in the inset. Figure 2g shows SEHRS results for ($I^{RCP} + I^{LCP}$) and ($I^{RCP} - I^{LCP}$) in the top and bottom panels, respectively. The former is simply the hyper-Raman spectrum of CV, as also shown in Fig. 1d (bottom). The latter demonstrates that there is no measurable CID on these achiral substrates, at stark contrast to the sign-changing peaks observable with nanohelices. Now, the key question is: does this sign change upon rotating the sample? If it does, the sign change would be indicative of extrinsic chirality and, hence, not a signature of hyper-Raman optical activity.

Figure 3a,b shows the SERS-CID and SEHRS-CID spectra of CV molecules on left- and right-handed nanohelices, for eight sample rotation angles (ϕ). Clearly, there are some fluctuations of the peak heights. These are attributed to millimetre-scale non-uniformity across the samples that results in variable CV concentration and quenching rates. Importantly, though, in both Raman and hyper-Raman scattering, the sign of the CID spectra is independent of sample rotation.

The data in Fig. 2c indicate four sign changes that are periodic. It is impossible for a set of eight equally spaced points (45° step) to exhibit the same sign with such a periodicity. Therefore, we conclude that the sign of the SERS-CID and SEHRS-CID spectra is independent of the sample rotation. This conclusion excludes extrinsic chirality, and it is consistent with the presence of an antisymmetric Raman tensors, characteristic of Raman optical activity and of hyper-Raman optical activity, respectively. For clarity, Fig. 3a,b focus on the most pronounced Raman and hyper-Raman peaks, in the 1,500–1,700 cm^{-1} region. The full 1,000–1,800 cm^{-1} region comprised three hyper-Raman peaks, and they all keep the same sign upon rotation, as shown in Supplementary Fig. 4. Moreover, while the data in Supplementary Fig. 4 were acquired in May 2023, rebuilding and recalibrating the experiment to repeat the measurements in February 2024 produced very similar results, as shown in Supplementary Fig. 5. The observed effects are robust, and they originate from a chirality conferral from the electromagnetic field of the plasmonic nanohelices to the achiral molecules. But how?

In the following, we identify all the lead mechanisms for the light–matter interactions that play a role in our experiments (Fig. 4) and we calculate their quantum amplitudes, whose modulus square relates to the hyper-Raman signal intensity that we measure. First, we consider the hyper-Raman process in the CV molecules. It involves the annihilation of two incident photons (at ω) and the emission of a Stokes frequency-shifted second-harmonic (at $\omega' = 2\omega - \omega_{vib}$), where ω_{vib} is the vibrational frequency of the CV molecule. In the electric dipole approximation, the molecular response depends on the vibrational derivative of the molecular hyperpolarizability that can be written as[38]

$$\beta'_{ijm} \equiv Q^{1\leftarrow 0}[\partial\beta_{ijm}(\omega)/\partial Q]|_{Q_0}. \tag{2}$$

Here and below, the prime symbol denotes a vibrational transition. The molecular hyperpolarizability tensor β for the input frequency ω (i,j and m are the Cartesian coordinates) comprises three terms corresponding to the three possible sequences of absorbing two photons and emitting one at the second-harmonic, in a molecule. Equation (2) uses the Taylor series expansion of the tensor in terms of the normal mode coordinate Q for the activated molecular vibration, whose matrix element $\langle 1|Q|0\rangle$ for a fundamental $1 \leftarrow 0$ transition is represented as $Q^{1\leftarrow 0}$. The hyperpolarizability derivative in square brackets is evaluated at the equilibrium configuration Q_0. The expression on the right-hand side of equation (2) couples with a product of input and output polarization vectors, $e_i(\omega)e_j(\omega)\bar{e}'_m(\omega')$, the overbar denoting complex conjugation where necessary for circular polarizations. Hence, for the CV molecules, the quantum amplitude takes the form $\beta'_{ijm}e_i(\omega)e_j(\omega)\bar{e}'_m(\omega')$, using the implied summation convention for repeated subscript indices. Next, we take the nanohelix into account.

In our data, the observed CID in the hyper-Raman signals can only be generated through coupling between the electromagnetic field generated by chiral Au nanohelices and the achiral CV molecules, where nearest-neighbour interactions can be assumed the strongest. Considering the nanohelix + CV molecule as an entity, each of the three-photon events can occur at either site, within the span of an optical wavelength. The dynamic coupling may be represented as a quasi-instantaneous two-body interaction. We consider the lowest non-vanishing order of perturbation theory to derive the quantum amplitude for the overall process—fourth order, comprising third order in single-centre light–matter interactions and first order in a two-centre coupling.

As our system is doubly resonant, we now consider the case where the two incident photons are annihilated in the nanohelix, and the hyper-Raman photon emerges from the CV; energy is conserved by near-field dynamic coupling between the two entities. There are 12 contributory pathways for this specific form of interaction, represented by the 12 topologically distinct diagrams shown in Fig. 4a. For gold, the world line is represented with a width as a visual aid, and its tensor response is a nonlinear susceptibility ($\chi^{(2)}_{Au}$) in contrast to the molecular response of the CV ($\tilde{\alpha}'_{CV}$), where tilde denotes values associated with input at the optical harmonic (2ω). For this form of interactions, we can write $\chi^{(2)}_{Au} \overset{\cap}{\underset{\cup}{}} \tilde{\alpha}'_{CV}$, where the symbol $\overset{\cap}{\underset{\cup}{}}$ denotes electrodynamic coupling. Corrective factors in the coupling, associated with plasmonic effects in the gold nanoparticles, are assimilated within the coupling tensors, as is shown for energy transfer by the methods of Schatz et al.[39–41]. In the electric dipole approximation, summing over all 12 contributions and over the repeated indices k, l, we obtain

$$\left\{\chi^{(2)}_{Au} \overset{\cap}{\underset{\cup}{}} \tilde{\alpha}'_{CV}\right\}_{ijm} \equiv \chi^{Au(2)}_{ijk}(-2\omega;\omega,\omega)V_{kl}(2\omega/c', \mathbf{R}_{CV} - \mathbf{R}_{Au})\,Q^{1\leftarrow 0}\left[\partial\alpha^{CV}_{lm}(2\omega)\Big/\partial Q\right]\Big|_{Q_0}, \tag{3}$$

where $\mathbf{R}_{CV}$ and $\mathbf{R}_{Au}$ represent the local position vectors of the CV and nanohelix, respectively, and where the c' denotes the local permittivity-corrected speed of light[42]. The expression on the right-hand side of equation (3) again couples with a product of input and output polarization vectors to give the first estimate of the quantum amplitude:

$$\left\{\chi^{(2)}_{Au} \overset{\cap}{\underset{\cup}{}} \tilde{\alpha}'_{CV}\right\}_{ijm} (\omega)e_j(\omega)\bar{e}'_m(\omega'). \tag{4}$$

https://doi.org/10.1038/s41566-024-01486-z

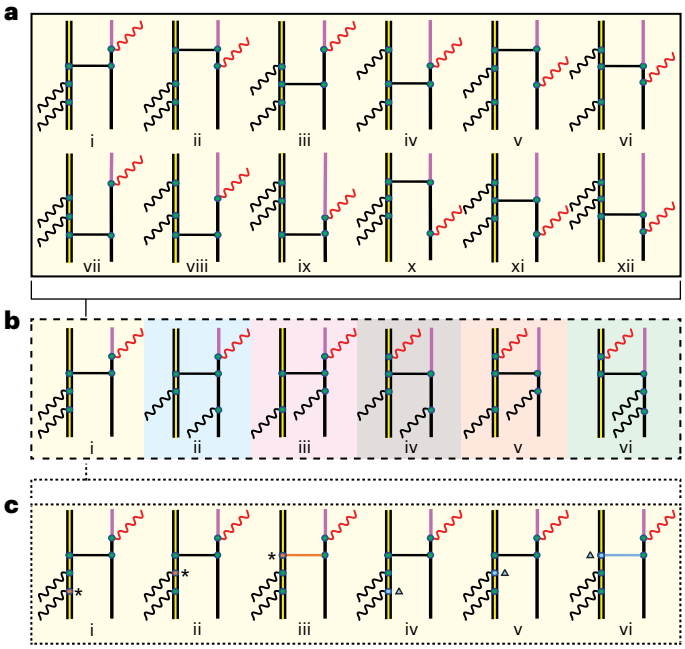

Fig. 4 | Feynman diagrams of the leading electrodynamic interactions that contribute to SEHRS. a, The 12 possible interactions when the two incident photons are annihilated at the nanohelix and a Raman-shifted photon is emitted at the CV molecules. Time progresses upwards. The Au nanohelix is represented by the vertical gold-coloured world line on the left in each case, its thickness signifying bulk response. The world line for the CV is represented by the black line on the right, its final state in purple exhibiting vibrational excitation. The input photons are shown as black wavy lines and the signal output photon as red, and each radiation field–matter interaction is shown as a green dot. The horizontal dashed line represents dynamic coupling in the near-zone limit. Line intervals between interaction dots on either side represent virtual states. **b**, The six possible permutations of annihilated and emitted photons. ii–vi illustrate different cases, with the same temporal ordering in which at least one of the input photon annihilations takes place within the CV, with iv–vi further distinguished by the emitted photon originating from the nanohelix. **c**, Leading forms of mixed-multipole counterparts to **b**(i). Here, the green dot signifies an E1 interaction, orange M1 and blue E2. For clarity, the M1 and E2 interactions are highlighted with an asterisk and a triangle, respectively. Similar counterparts exist for each of the remaining subpanels within **b**.

In equation (3), V designates the retarded resonance dipole–dipole interaction, a second rank tensor whose argument exhibits explicit dependence on frequency and the vector displacement of the CV molecule from its counterpart nanohelix. However, within the near-zone the leading term of the tensor is frequency independent[43] and we can approximate the result in terms equivalent to static coupling $V_{kl}(2\omega/c', \mathbf{R}_{CV} - \mathbf{R}_{Au}) \simeq V^0_{kl}(\mathbf{R}_{CV} - \mathbf{R}_{Au})$. Equation (3) features the Raman tensor for the CV, the quantity in square brackets denoting the mode derivative of the polarizability at the equilibrium configuration.

Figure 4b highlights the fact that, although we expect the doubly resonant system to favour photon annihilations at the helix and emission at the CV molecule, other annihilation-emission photon events are possible and they cannot be distinguished, under much less than the span of a wavelength. Each of the 12 diagrams in Fig. 4a has four counterparts with the same temporal sequence but differently positioned photon events. The full forms of associated general equations are the subject of a follow-up publication, where we further discuss additional quantum amplitudes contributions and the reasons why they have been omitted.

Within the E1 approximation, no CID can arise. The tensor response of the complete material system is an eigenstate of the spatial parity operation P with eigenvalue −1; it does not register chirality because it is specifically odd parity[44]. Therefore, we now need to focus on additional terms arising from electric and magnetic multipole expansions and the symmetry-based selection rules. We have the following leading terms in the Power–Zienau–Woolley interaction Hamiltonian:

$$H_{\text{int}}^{\text{mult}} = \underbrace{-\boldsymbol{\mu}\cdot\mathbf{e}^{\perp}}_{\text{E1}} \underbrace{-\mathbf{m}\cdot\mathbf{b}}_{\text{M1}} \underbrace{-\boldsymbol{\Theta}:\boldsymbol{\nabla}\mathbf{e}^{\perp}}_{\text{E2}} - \ldots, \tag{5}$$

where $\mathbf{e}^{\perp}$ is the transverse electric field and $\mathbf{b}$ the magnetic field. The magnetic dipole (M1) and electric quadrupole (E2) terms, whose moments are denoted by $\mathbf{m}$ and $\boldsymbol{\Theta}$, respectively, connect to the first order of expansion in the vector potential[45,46]. The transverse electric field $\mathbf{e}^{\perp}$ is a polar vector, odd under P, as is the electric dipole $\mathbf{m}$ with which it couples. In the M1 term, both the field $\mathbf{b}$ and the magnetic dipole $\mathbf{m}$ are pseudovectors, even under P; so too is the electric quadrupole $\boldsymbol{\Theta}$, a second-rank tensor coupled to the gradient of the electric field. M1 and E2 represent interactions whose associated magnitudes are small compared with E1 if selection rules simultaneously allow both, which requires symmetry breaking. In consequence, both are commonly engaged, together with E1, in chiral interactions.

Each field–matter interaction (green dot) entails all of the contributions given in equation (5)—not just the first. Moreover, the hyper-Raman signal intensity arises from the modulus square of the quantum amplitude. In consequence, the leading contribution to any chiroptically responsive, enantioselective effect comprises a sum of cross-terms between the leading, fully E1 quantum amplitude contribution associated with equation (2) and terms of the forms exhibited by equation (4) but in which one of the E1 interactions is substituted by an M1 or E2 coupling. Those substitute interactions must occur at the Au site since that is the sole chiral constituent. In this case, the relevant counterparts to Fig. 4b(i), for example, are as shown in Fig. 4c.

Each of the graphs in Fig. 4c again has a counterpart within the other 71 time orderings. When the quantum amplitudes for the full set are summed, in the back-directed Raman signal, we obtain the terms whose sign changes with the handedness of circularly polarized light and upon substituting the opposite enantiomorph of the nanohelix. It is these terms that contribute to the signal measured in our experiments (for the full details of these calculations, see ref. 47).

Because hyper-Raman scattering (and therefore hyper-Raman scattering optical activity) probes different physical quantities (hyperpolarizabilities) than Raman scattering, it offers complementary vibrational information[48]. For instance, it can reveal vibrational modes that are silent in Raman scattering[49]. In microscopy of biological systems, it combines increased penetration depth from convenient excitation in the near-infrared (NIR) transparent region with detection in the visible[47,50]; the process also offers reduced (one-photon) autofluorescence and lower photochemical damage, since illumination is away from most electronic resonances[51]. Importantly, hyper-Raman scattering benefits from better enhancement at the surface of plasmonic nanoparticles and nanostructures[52], because it scales as a power law of the local electric fields[53]. Hyper-Raman scattering is particularly suited for studying molecules with strong hyperpolarizabilities, such as push–pull organic chromophores[54]; it offers a broader range of pH sensitivity for molecular imaging inside cells[55], and because it requires two incident photons, it can benefit from entangled photon states[56].

Similarly to Raman optical activity, hyper-Raman optical activity can be expected to reveal the absolute configuration or conformation, in proteins, in synthetic chiral polymers and in similarly intricate molecules. This is important in chiral molecules, especially in pharmaceuticals, agrochemicals, natural products and bioactive compounds are often large, with complex geometries, containing numerous chiral centres that each require analysis. Typically, these centres are chiral carbons bonded to functional groups, such as nitriles[57] or amines[58–60].

Experimental methods that can distinguish and characterize the chirality within such molecules are highly desirable[61].

In conclusion, we report chirality conferral from the electromagnetic field of gold nanohelices to achiral molecules, the former being over 100 times larger than the latter. This conferral has enabled the experimental observation of the hyper-Raman optical activity effect that was theoretically predicted 45 years ago. The observation has now been demonstrated in a doubly resonant system, consisting of plasmonic gold nanohelices and CV molecules, where the chirality of the nanohelices was conferred to the achiral (on average) molecules. Care has been taken to eliminate possible artefacts, for example, from extrinsic chirality in the nanohelices, from the degree of light circularity, from photodecomposition and from differences in the number of illuminated molecules. When achiral nanoparticles were used as the SERS substrate (also see Supplementary Fig. 6), the hyper-Raman optical activity effect was absent, confirming the role of chirality transfer from the nanohelices. The origin of the effect was revealed by identifying the lead light–matter interaction processes and by calculating their quantum amplitudes, whose modulus square produces the hyper-Raman signal intensity observed. We show that the chiroptical response originates from the sum of cross-terms between the leading, fully electric dipole quantum amplitude contribution and terms that include contributions from magnetic dipoles or electric quadrupoles.

Our findings show that the chirality conferral mechanism between chiral nanoparticles and achiral molecules is highly promising for exploring new science at the organic–inorganic interface, as demonstrated by the discovery of a new physical effect. We anticipate that hyper-Raman optical activity will be sensitive to the absolute configuration of chiral molecules that are key for synthetic biology, for human-made self-assembling nanotechnology, and for pharmaceutical synthesis. Naturally, as it has taken 45 years between the prediction of this effect and its first observation, the technological development of the associate experimental technique and its commercialization will take time. Important milestones will be to observe hyper-Raman optical activity in chiral molecules and in those that are of biomedical relevance. Further optimization of SERS materials and substrates can lead to even greater enhancements in Raman signals, enabling the detection and analysis of even lower concentrations of analytes. Exploring new fabrication techniques and materials with enhanced plasmonic properties can contribute to this optimization. Exploring machine learning algorithms and chemometric methods can aid in the design and synthesis of SERS materials as well as intrinsically chiral molecules that meet the above criteria. Optimizing the light sources for this emerging technique will also be a key advance.

Online content

Any methods, additional references, Nature Portfolio reporting summaries, source data, extended data, supplementary information, acknowledgements, peer review information; details of author contributions and competing interests; and statements of data and code availability are available at https://doi.org/10.1038/s41566-024-01486-z.

References

1. Liu, Z. et al. Harnessing chemical energy for the activation and joining of prebiotic building blocks. *Nat. Chem.* **12**, 1023–1028 (2020).
2. Gianga, T. M. & Pantoş, G. D. Structurally divergent dynamic combinatorial chemistry on racemic mixtures. *Nat. Commun.* **11**, 3528 (2020).
3. Wang, H.-F. et al. Networks with controlled chirality via self-assembly of chiral triblock terpolymers. *Sci. Adv.* **6**, eabc3644 (2020).
4. Jolliffe, J. Catalytic enantioselective synthesis of atropisomeric biaryls by a cation-directed *O*-alkylation. *Nat. Chem.* **9**, 558–562 (2017).
5. Lu, J. et al. Enhanced optical asymmetry in supramolecular chiroplasmonic assemblies with long-range order. *Science* **371**, 1368–1374 (2021).
6. Xu, Y. & Zhu, T. F. Mirror-image T7 transcription of chirally inverted ribosomal and functional RNAs. *Science* **378**, 405–412 (2022).
7. Jiang, W. et al. Emergence of complexity in hierarchically organized chiral particles. *Science* **368**, 642–648 (2020).
8. Huang, S. et al. Supramolecular chirality transfer toward chiral aggregation: asymmetric hierarchical self-assembly. *Adv. Sci.* **8**, 2002132 (2021).
9. Cao, Z. et al. Chirality transfer from sub-nanometer biochemical molecules to sub-micrometer plasmonic metastructures: physiochemical mechanisms, biosensing, and bioimaging opportunities. *Adv. Mater.* **32**, 1907151 (2020).
10. Ostovar pour, S. et al. Through-space transfer of chiral information mediated by a plasmonic nanomaterial. *Nat. Chem.* **7**, 591–596 (2015).
11. Zhang, Q. et al. Unraveling the origin of chirality from plasmonic nanoparticle–protein complexes. *Science* **365**, 1475–1478 (2019).
12. Lee, H. E. et al. Amino-acid- and peptide-directed synthesis of chiral plasmonic gold nanoparticles. *Nature* **556**, 360–365 (2018).
13. Jana, M. K. et al. Organic-to-inorganic structural chirality transfer in a 2D hybrid perovskite and impact on Rashba-Dresselhaus spin–orbit coupling. *Nat. Commun.* **11**, 4699 (2020).
14. Long, G. et al. Spin control in reduced-dimensional chiral perovskites. *Nat. Photon.* **12**, 528–533 (2018).
15. Ji, L. et al. Cooperative chirality and sequential energy transfer in a supramolecular light-harvesting nanotube. *Angew. Chem. Int. Ed.* **58**, 844–848 (2019).
16. Ben-Moshe, A. et al. The chain of chirality transfer in tellurium nanocrystals. *Science* **372**, 729–733 (2021).
17. Stetsovych, O. et al. From helical to planar chirality by on-surface chemistry. *Nat. Chem.* **9**, 213–218 (2017).
18. Goubert, G. et al. Monitoring interconversion between stereochemical states in single chirality-transfer complexes on a platinum surface. *Nat. Chem.* **9**, 531–536 (2017).
19. Kim, Y. et al. Reconfigurable chiroptical nanocomposites with chirality transfer from the macro- to the nanoscale. *Nat. Mater.* **15**, 461–468 (2016).
20. Jones, R. R. et al. Dense arrays of nanohelices: Raman scattering from achiral molecules reveals the near-field enhancements at chiral metasurfaces. *Adv. Mater.* **35**, 2209282 (2023).
21. Kartau, M. et al. Chiral metafilms and surface enhanced Raman scattering for enantiomeric discrimination of helicoid nanoparticles. *Adv. Opt. Mater.* **11**, 2202991 (2023).
22. Xiao, X. et al. Plasmonic polarization rotation in SERS spectroscopy. *Nano Lett.* **23**, 2530–2535 (2023).
23. Kim, J.-Y. et al. Assembly of gold nanoparticles into chiral superstructures driven by circularly polarized light. *J. Am. Chem. Soc.* **141**, 11739–11744 (2019).
24. Andrews, D. L. & Thirunamachandran, T. Hyper-Raman scattering by chiral molecules. *J. Chem. Phys.* **70**, 1027–1030 (1979).
25. Marble, C. B. et al. Hyper-Raman optical activity of biologically relevant chiral molecules. In *Proc. SPIE 11288, Quantum Sensing and Nano Electronics and Photonics XVII* 1128829 (SPIE, 2020).
26. Liu, Y. et al. Detection and analysis of chiral molecules as disease biomarkers. *Nat. Rev. Chem.* **7**, 355–373 (2023).
27. Machalska, E. et al. Recognition of the true and false resonance Raman optical activity. *Angew. Chem. Int. Ed.* **60**, 21205–21210 (2021).
28. Hooper, D. C. et al. Strong rotational anisotropies affect nonlinear chiral metamaterials. *Adv. Mater.* **29**, 1605110 (2017).
29. Collins, J. T. et al. Second-harmonic generation optical rotation solely attributable to chirality in plasmonic metasurfaces. *ACS Nano* **12**, 5445–5451 (2018).

30. Banik, M. et al. Orientation-dependent handedness of chiral plasmons on nanosphere dimers: how to turn a right hand into a left hand. *ACS Photonics* **3**, 2482–2489 (2016).
31. Barron, L. D. & Buckingham, A. D. Rayleigh and Raman optical activity. *Annu. Rev. Phys. Chem.* **26**, 381–396 (1975).
32. Barron, L. D. A vibronic theory of the Raman effect and its application to antisymmetric resonance Raman scattering. *Mol. Phys.* **31**, 129–145 (1976).
33. Lacinska, E. M. et al. Raman optical activity of 1T-TaS_2. *Nano Lett.* **22**, 2835–2842 (2022).
34. Kelley, A. M. Hyper-Raman scattering by molecular vibrations. *Annu. Rev. Phys. Chem.* **61**, 41–61 (2010).
35. Barron, L. D. True and false chirality and parity violation. *Chem. Phys. Lett.* **123**, 423–427 (1986).
36. Verbiest, T., Kauranen, M., Van Rompaey, Y. & Persoons, A. Optical activity of anisotropic achiral surfaces. *Phys. Rev. Lett.* **77**, 1456–1459 (1996).
37. Plum, E. et al. Metamaterials: optical activity without chirality. *Phys. Rev. Lett.* **102**, 113902 (2009).
38. Long, D. A. & Stanton, L. Studies of nonlinear phenomena. I. Theory of the hyper Raman effect. *Proc. R. Soc. A* **318**, 441–457 (1970).
39. Hsu, L.-Y., Ding, W. & Schatz, G. C. Plasmon-coupled resonance energy transfer. *J. Phys. Chem. Lett.* **8**, 2357–2367 (2017).
40. Ding, W., Hsu, L.-Y. & Schatz, G. C. Plasmon-coupled resonance energy transfer: a real-time electrodynamics approach. *J. Chem. Phys.* **146**, 064109 (2017).
41. Ding, W., Hsu, L.-Y., Heaps, C. W. & Schatz, G. C. Plasmon-coupled resonance energy transfer II: exploring the peaks and dips in the electromagnetic coupling factor. *J. Phys. Chem. C* **122**, 22650–22659 (2018).
42. Juzeliūnas, G. Molecular-radiation and molecule–molecule processes in condensed media: a microscopic QED theory. *Chem. Phys.* **198**, 145–158 (1995).
43. Scholes, G. D. & Andrews, D. L. Damping and higher multipole effects in the quantum electrodynamical model for electronic energy transfer in the condensed phase. *J. Chem. Phys.* **107**, 5374–5384 (1997).
44. Andrews, D. L. Quantum formulation for nanoscale optical and material chirality: symmetry issues, space and time parity, and observables. *J. Opt.* **20**, 033003 (2018).
45. Craig, D. P. & Thirunamachandran, T. *Molecular Quantum Electrodynamics: An Introduction to Radiation-Molecule Interactions* (Dover Publications, 1998).
46. Woolley, R. G. *Foundations of Molecular Quantum Electrodynamics* (Cambridge Univ. Press, 2022).
47. Madzharova, F. et al. Gold- and silver-coated barium titanate nanocomposites as probes for two-photon multimodal microspectroscopy. *Adv. Funct. Mater.* **29**, 1904289 (2019).
48. Yu, C. C. et al. Vibrational couplings and energy transfer pathways of water's bending mode. *Nat. Commun.* **11**, 5977 (2020).
49. Kaur, G. et al. Mapping the real-time vibrational infrastructure of Cs_2SnI_6 nanocrystals through coherent phonon dynamics. *ACS Photonics* **9**, 2756–2766 (2022).
50. Leng, W. & Kelley, A. M. Surface-enhanced hyper-Raman spectra and enhancement factors for three SERS chromophores. SEHRS spectra on Ag films at pulse energies below 2 pJ. *J. Am. Chem. Soc.* **128**, 3492–3493 (2006).
51. Heiner, Z. et al. Bio-probing with nonresonant surface-enhanced hyper-Raman scattering excited at 1,550 nm. *J. Raman Spectrosc.* **52**, 394–403 (2021).
52. Madzharova, F. et al. Plasmon enhanced two-photon probing with gold and silver nanovoid structures. *Adv. Optical Mater.* **7**, 1900650 (2019).
53. Madzharova, F., Heinera, Z. & Kneipp, J. Surface enhanced hyper Raman scattering (SEHRS) and its applications. *Chem. Soc. Rev.* **46**, 3980–3999 (2017).
54. Kelley, A. M., Leng, W. & Blanchard-Desce, M. Resonance hyper-Raman scattering from conjugated organic donor–acceptor "push–pull" chromophores with large first hyperpolarizabilities. *J. Am. Chem. Soc.* **125**, 10520–10521 (2003).
55. Kneipp, J. et al. One- and two-photon excited optical pH probing for cells using surface-enhanced Raman and hyper-Raman nanosensors. *Nano Lett.* **7**, 2819–2823 (2007).
56. Chen, F. & Mukamel, S. Vibrational hyper-Raman molecular spectroscopy with entangled photons. *ACS Photonics* **8**, 2722–2727 (2021).
57. Song, L. et al. Dual electrocatalysis enables enantioselective hydrocyanation of conjugated alkenes. *Nat. Chem.* **12**, 747–754 (2020).
58. Xi, Y., Ma, S. & Hartwig, J. F. Catalytic asymmetric addition of an amine N–H bond across internal alkenes. *Nature* **588**, 254–260 (2020).
59. Thorpe, T. W. et al. Multifunctional biocatalyst for conjugate reduction and reductive amination. *Nature* **604**, 86–91 (2022).
60. Chen, J. J. et al. Enantioconvergent Cu-catalysed N-alkylation of aliphatic amines. *Nature* **618**, 294–300 (2023).
61. Brázda, P. et al. Electron diffraction determines molecular absolute configuration in a pharmaceutical nanocrystal. *Science* **364**, 667–669 (2019).

Publisher's note Springer Nature remains neutral with regard to jurisdictional claims in published maps and institutional affiliations.

Open Access This article is licensed under a Creative Commons Attribution 4.0 International License, which permits use, sharing, adaptation, distribution and reproduction in any medium or format, as long as you give appropriate credit to the original author(s) and the source, provide a link to the Creative Commons licence, and indicate if changes were made. The images or other third party material in this article are included in the article's Creative Commons licence, unless indicated otherwise in a credit line to the material. If material is not included in the article's Creative Commons licence and your intended use is not permitted by statutory regulation or exceeds the permitted use, you will need to obtain permission directly from the copyright holder. To view a copy of this licence, visit http://creativecommons.org/licenses/by/4.0/.

© The Author(s) 2024

Methods

Definition of circularly polarized light

Here, we define LCP as follows: looking from the point of view of the source, along the direction of propagation, the electric field of LCP light traces a helix in the space that curls anti-clockwise.

Metasurface fabrication

Nanohelices were grown using the nano glancing angle deposition (nanoGLAD) technique. Small gold (Au) dots were arranged in a hexagonal pattern on a silicon (Si) wafer, acting as seed for growth. The substrates were cooled to 90 K and tilted at an angle of 87°. Co-deposition of metals resulted in alloyed nanohelices (96% Au, 4% Cu). A quartz crystal microbalance monitored deposition rates, allowing control over the alloy ratio. Metal vapour impinged on the surface, causing nanohelices to grow by rotating the surface. The direction of rotation determined the nanohelices' handedness. Further details of the nanoGLAD fabrication process can be found in refs. 62,63.

Achiral SERS substrate

Silicon (Si) nanopillars topped with gold (Au) nanoparticles were purchased from Silmeco. These Au-topped nanopillars are fabricated through maskless plasma etching of Si wafers followed by electron beam evaporation of Au to form the nanoparticle tops. Further details on the fabrication process of the substrate can be found in ref. 64. The substrate formed on 3 mm × 3 mm Si wafer was then spin-coated with 0.6 mM CV in ethanol solution.

Material characterization

The SEM and STEM micrographs shown in Fig. 1e were captured using a JEOL JSM-7900F Schottky Field Emission SEM. For SEM, an acceleration voltage of 10 kV and a working distance of approximately 3–3.5 mm were employed. For STEM, a small square of nanohelices on a silicon wafer (approximately 10 mm^2) was cut and sonicated in 0.7 ml of chloroform for 20 min before being deposited (a few microlitres) onto Formvar STEM grids. The STEM images were obtained using an acceleration voltage of 30 kV and a working distance of around 10.5 mm.

Reflectance CD spectroscopy

Reflectance CD spectra of the clean (no CV) nanohelix arrays shown in Fig. 2a–c and Supplementary Fig. 2 were acquired using a Zeiss Axio imager M2m wide-field microscope. The illumination source consisted of white light generated by a halogen filament lamp, which was circularly polarized using a motorized wire-grid polarizer and an achromatic quarter waveplate. Visible spectroscopy (400–800 nm) and NIR spectroscopy (900–2,100 nm) were performed using different $\lambda/4$ waveplates. Illumination of the sample was achieved using an EpiPlan-Neofluar 5×/0.15 HD DIC objective, and the spectra were collected in bright-field reflection mode. The reflected light was then directed through an analysing polarizer. Subsequently, the light was transmitted through a multimode fibre with a core diameter of 200 µm (numerical aperture 0.22) to either an Ocean Optics QE Pro spectrometer (for the visible range) or an Ocean Optics NIRQuest spectrometer (for the NIR range).

To quantify the CD at each rotational position, the ellipticity (θ) parameter was calculated using $\theta = \frac{180}{\pi}\tan^{-1}\left[\left(\sqrt{I^{RCP}} - \sqrt{I^{LCP}}\right)/\left(\sqrt{I^{RCP}} + \sqrt{I^{LCP}}\right)\right]$, where I^{RCP} and I^{LCP} represent the intensities of detected light for RCP and LCP illumination, respectively.

To capture the angular dependence of ellipticity on the orientation of the nanohelix arrays, reflectance spectra were obtained at discrete sample rotation positions ranging from 0° to 360° with 20° intervals. Supplementary Fig. 2b shows the reflectance CD spectra averaged for both LCP and RCP data at each rotational position. For the visible range, 200 spectra were acquired and averaged at each rotation, while for the NIR range, 1,000 spectra were obtained and averaged. The integration time per spectrum was set to 100 ms.

Figure 2c illustrates the ellipticity at 532 nm and 1,064 nm as a function of sample rotation. The rotational averages are depicted in Fig. 2b.

Absorption spectroscopy

CV powder purchased from Sigma-Aldrich was used to form a solution with an analyte concentration of 0.3 mM in ethanol.

An Applied Photophysics Chirascan equipped with an avalanche photodetector was used to collect the absorption spectra presented in Fig. 1c of the main text. To distinguish the absorbance of the CV from that of the ethanol reference spectra of pure ethanol were taken. These spectra were used to subtract the ethanol contributions from the final spectra, leaving only the contributions from the CV.

The CV 0.3 mM solution was added to a 1 cm ml^{-1} cuvette. Absorption spectra were taken with a step size and bandwidth of 1 nm with ranges from 900 to 1,100 nm and 450 to 900 nm. High signal strength in the 450–900 nm range led to oversaturation of the detector. The 0.3 mM solution was diluted by 100× to 3 µM and measurements in the 450–900 nm range were repeated with the same parameters.

Analyte preparation

CV powder was purchased from Sigma-Aldrich. A solution with an analyte concentration of 0.3 mM was prepared in ethanol. To achieve uniform distribution and maximize the amount of analyte on the surface for optimal hyper-Raman signal, 500 µl of the 0.3 mM CV in ethanol solution was deposited during a 20 s spin step at 700 rpm, followed by a 60 s spin step at 1,500 rpm. This spin and deposition cycle was repeated three times. A Laurell spin coater (WS-650Mz-23NPPB) was used for the spin-coating process. After the spin steps, the samples were allowed to dry naturally under atmospheric conditions inside the spin coater before being removed.

Simulations

Simulations of the nanohelices were performed using finite-difference time-domain simulations in ANSYS-Lumerical.

In Supplementary Fig. 1, the finite-difference time-domain simulation region encompassed dimensions of 310 nm in the x axis, 410 nm in the y axis and 390 nm in the z axis, using perfectly matched layer boundary conditions. To account for the effects of nearest neighbour interaction, a pair of nanohelices on a Si/SiO_2 substrate was simulated, with a separation corresponding to the hexagonal array (120 nm). The nanohelices were generated using Autodesk Inventor, providing a realistic representation of the structures.

In the simulations, a pair of polarized total-field scattered-field (TFSF) light sources spanning a range from 400 nm to 1.6 µm were employed in Lumerical. A scattered field analysis group was employed to observe the scattering cross-section. The TFSF regions, with dimensions of 270 nm in the x axis, 370 nm in the y axis and 330 nm in the z axis, were defined with a mesh refinement of 5 nm in each dimension.

Circular polarization was achieved by superposing the TFSF regions with perpendicular polarization and a $\lambda/4$ phase offset. This phase offset allowed for the simulation of LCP or RCP by shifting the phase by ±90°. By analysing the electric field strength, data were extracted for the 532 nm and 1,064 nm electromagnetic modes from the plane bisecting through both nanohelices, specifically the x–z plane (as shown in Supplementary Fig. 1).

Circular hyper-Raman spectroscopy

The modified Renishaw inVia Raman microscope used in this study has the capability of performing hyper-Raman scattering measurements with circularly polarized light. The incident light source at 1,064 nm was provided by the idler of a Spectra-Physics Inspire optical parametric oscillator (INSPIRE HF 100) pumped by a femtosecond Ti:Sapphire laser (MAI TAI HP 1040S). The 1,064 nm laser pulse repetition rate was 80 MHz, with a pulse duration of approximately 180 fs,

corresponding to a Fourier transform limited spectral bandwidth of $\Delta\lambda \approx 15$ nm ($\Delta K \approx 140$ cm^{-1}) at 1,064 nm.

The bandwidth of a femtosecond pulsed laser system ($\Delta K \approx 140$ cm^{-1} at 1,064 nm) is too large to adequately resolve features in Raman and hyper-Raman spectra, which typically require spectral resolving power in the region of 10 cm^{-1} to 20 cm^{-1} (refs. 34,65). To frequency narrow our laser source to a level suitable for hyper-Raman spectroscopy, a frequency narrowing system was employed. The frequency narrowing system is illustrated in Supplementary Fig. 3a and was designed according to ref. 66. The size of the setup is determined by the focal length (f) of the spherical mirror (Au $f = 750$ mm) and the number of lines per mm in the grating (1,200 lines mm^{-1}). The bandwidth of the laser can be controlled by adjusting the slit width. For this study, a slit width of 2.5 mm was employed, providing a SEHRS spectral resolving power of 14.5 cm^{-1}, as indicated by the hyper-Rayleigh spectrum of ZnSe in Supplementary Fig. 3b. A pair of lenses were used to collimate the beam and optimize the power throughput to the inVia system. Additionally, a 1,064 nm zero-order $\lambda/2$ plate was positioned before the 4f-line system to optimize the incident polarization onto the diffraction grating and enhance the power throughput (Supplementary Fig. 3a).

An Olympus LUMPlanFL N 60× water immersion objective with a numerical aperture of 1.0 was employed. A glass cover slip was placed over the substrate; deionized water served as the immersion medium. Within the inVia system, a secondary beam expander (Fig. 2d) provided control over the laser spot diameter and, thus, the irradiance of the 1,064 nm light at the sample. A short-pass filter with an ~910 nm edge wavelength was used as a dichroic mirror to direct the 1,064 nm light onto the sample, while allowing the hyper-Rayleigh and hyper-Raman light to pass through to the spectrometer. The spectrometer used a 1,024 × 256 pixel charge-coupled device (CCD) detector cooled to −70 °C and a blazed 1,800 lines mm^{-1} diffraction grating.

The laser spot was deliberately defocused using lenses (L_1 and L_2) shown in Fig. 2d to distribute the laser power over a larger area compared to fully focused conditions. This reduction in laser irradiance helped minimize quenching effects, which can diminish SERS and SEHRS and ultimately introduce bias in CID measurements. It is worth noting that the collection optics were maintained at the image focus of the sample surface, where detection is optimized. To estimate the defocused laser diameter for computing the irradiance, the hyper-Rayleigh intensity was measured while scanning the defocused laser spot (in a line map) over the sharp edge of a 1 µm layer of ZnSe on GaAs sample. This is illustrated in Supplementary Fig. 3c,d. The estimated laser spot diameter was found to be 3.3 ± 0.2 µm. The laser power under the objective was measured to be 1.1 ± 0.1 mW using a Thorlabs S175C Microscope Slide Thermal Power Sensor. The corresponding irradiance was computed as (13 ± 2) kW cm^{-2}.

To align and optimize circularly polarized light at the sample surface, the polarization (polarizer and analyser) optics for SEHRS were aligned for vertical polarization before mounting the control $\lambda/4$ waveplate (u-optic, super-achromatic $\lambda/4$ waveplate; 380–1,100 nm) to the motor (Thorlabs Motorized Precision Rotation Mount PRM1Z8). A zero-order $\lambda/4$ waveplate (1,064 nm for SEHRS and 532 nm for SERS) and wire-grid polarizer were placed in tandem above a Si-amplified photodetector (Thorlabs; PDA100A-EC, 340–1,100 nm) at the sample plane, with the appropriate relative angle to filter out LCP or RCP. By measuring the time average voltage readout from a Tektronix oscilloscope, the angle of the control $\lambda/4$ waveplate was swept and plotted to find a minimum in the measured power. By fitting a weighted smoothed cubic spline through the data, the precise angle of the control $\lambda/4$ waveplate for LCP and RCP at the sample surface could be achieved. Supplementary Fig. 3e, f shows the measured voltage versus the absolute motor position (of the control $\lambda/4$ waveplate shown in Fig. 2d) for the SEHRS setup as an example. The system was checked for measurement bias between LCP and RCP by measuring the strength of the 520 cm^{-1} Raman phonon of Si (001) (Γ-point phonon) for SERS and the strength of the hyper-Rayleigh signal from polycrystalline ZnSe for SEHRS. All optimization data can be found in the University of Bath repository (see 'Data availability' statement).

Due to quenching effects, measurements of CID could not be taken repetitively from a single location. Therefore, 5 × 6 point maps (grid size 25 µm × 30 µm, point separation 5 µm) were acquired to measure the CID in SEHRS, with a 5 s acquisition time per map point. Cosmic ray removal was performed through nearest-neighbour cross-correlation post processing. The maps were scanned in a checkerboard pattern, switching the handedness of light when moving to the next map point. This sequencing allowed for the collection of all circular Raman information from a single map and helped minimize stochastic effects from variations in molecule concentration across the surface and changes in focus (laser and detection optics) on the sample. This approach is more advanced than acquiring separate RCP and LCP maps at different locations, which can lead to stochastic effects in CID from inconsistencies in experimental conditions (for example, variations in molecular concentration and/or surface quality, changes in optical focusing and so on; see ref. 20). The automation of this process was achieved using a LabVIEW VI, which controlled the inVia Raman microscope's acquisition and stage position while switching the handedness of light with the Thorlabs motorized mount ($\lambda/4$ waveplate shown in Fig. 2d). The samples were measured at rotational orientations between 0° and 360° in 45° intervals, azimuthal axis of rotation. For each orientation, three checkerboard maps were acquired from different areas on the sample to avoid quenching effects. These maps were then averaged for each angle. Each CID spectrum shown in Fig. 3 represents the average of three checkerboards per orientation. In Fig. 2f, all azimuthal orientations and checkerboards are averaged.

Supplementary Fig. 3g shows a time history of the power (voltage from Si-amplified detector) for the SEHRS pulsed laser. The proportional–integral–derivative controller clearly results in cyclic power fluctuations, and thus, the integration time for SEHRS-CID measurements was always set to 5 s to ensure that, on average over many acquisitions, the cyclic fluctuation of the laser power did not introduce experimental uncertainty.

Circular Raman spectroscopy

The modified inVia Raman microscope is also capable of linear Raman spectroscopy using circularly polarized light. For this purpose, a continuous-wave narrow-bandwidth 532 nm laser (Cobolt RL532-08; 50 mW) served as the incident light source. The irradiated light and back-scattered Raman light were focused and collected using an N-plan 50× objective with a numerical aperture of 0.75 in air. The spectrometer slit width was set to 65 µm, resulting in a spectral resolution of 1.6 cm^{-1}. The acquisition parameters and checkerboard mapping approach were identical to those employed for hyper-Raman CID measurements.

The laser power was attenuated to 0.10 (±0.01) mW under the objective. Similarly to hyper-Raman measurements, the laser focus spot diameter on the sample surface was deliberately increased using a pair of motorized lenses (L_1 and L_2) to mitigate quenching effects. The spot diameter was measured to be 4.0 (±0.3) µm by scanning the laser spot over a masked area of a Si wafer (following the procedure outlined in reference ref. 65). The corresponding irradiance was estimated to be 795 (±143) W cm^{-2}. Although the continuous-wave laser used for linear Raman measurements provided stable power (in contrast to the Inspire laser shown in Supplementary Fig. 3g), the integration time at each sample point was maintained at 5 s for consistency with the hyper-Raman measurements.

Data availability

The data that support the findings of this study are openly available in the repository of the University of Bath at https://doi.org/10.15125/BATH-01285.

References

62. Ohnoutek, L. et al. Second harmonic Rayleigh scattering optical activity of single Ag nanohelices in a liquid. *Nanoscale* **14**, 3888–3898 (2022).
63. Jeong, H.-H. et al. Dispersion and shape engineered plasmonic nanosensors. *Nat. Commun.* **7**, 11331 (2016).
64. Schmidt, M. S. et al. Large area fabrication of leaning silicon nanopillars for surface enhanced Raman spectroscopy. *Adv. Mater.* **24**, OP11–OP18 (2012).
65. Kelley, A. M. Resonance Raman and resonance hyper-Raman intensities: structure and dynamics of molecular excited states in solution. *J. Phys. Chem. A* **112**, 11975–11991 (2008).
66. Monmayrant, A., Weber, S. & Chatel, B. A newcomer's guide to ultrashort pulse shaping and characterization. *J. Phys. B* **43**, 103001 (2010).

Acknowledgements

Helpful comments from D. Bradshaw and K. Forbes are gratefully acknowledged. We are also grateful to L. Barron for the helpful discussion. The authors acknowledge support from Renishaw Plc (Wotton-under-Edge) and the Material and Chemical Characterisation Facility (MC^2, University of Bath). The authors also thank P. Fletcher, J. Masters, D. Lednitzky, P. Paluch, J. Mills and A. Moore, Dept. of Physics, University of Bath, for their technical support and W. Liu in the Dept. of Chemistry, University of Bath, for his assistance with spin-coating. D.W. and V.K.V. acknowledge support from Engineering and Physical Sciences Research Council iCASE EP/T517495/1. V.K.V. acknowledges support from Engineering and Physical Sciences Research Council grant EP/T001046/1, and the Royal Society University Research Fellowships RGF\EA\180228. L.Z. and V.K.V. acknowledge support from Royal Society grant ICA/R1/201088. R.J., G.D.P. and V.K.V. acknowledge support from the Leverhulme Trust Research Grant RP-G202-2-344. G.D.P. acknowledges support from the University of Bath Major Equipment Fund VB-FS1RCU.

Author contributions

Conceptualization: R.R.J. and V.K.V. Methodology: R.R.J., J.F.K. and H.K. Experimental investigation: R.R.J., J.F.K., S.R.C., R.J. and E.P. Experimental equipment: G.D.P., P.F., D.W. and V.K.V. Theory: D.L.A. Numerical simulations: R.R.J. and E.P. Samples: H.K. and P.F. Visualization: R.R.J., D.L.A. and V.K.V. Funding acquisition: B.S., T.B., L.Z., D.W. and V.K.V. Project administration: D.W. and V.K.V. Supervision: B.S., T.B., P.F., G.D.P., D.W. and V.K.V. Writing—original draft: R.R.J. Writing—review and editing: R.R.J., J.F.K., H.K., S.R.C., R.J., E.P., L.Z., G.D.P., B.S., T.B., P.F., D.W., D.L.A. and V.K.V.

Competing interests

The authors declare that they have no competing interests.

Additional information

Supplementary information The online version contains supplementary material available at https://doi.org/10.1038/s41566-024-01486-z.

Correspondence and requests for materials should be addressed to Ventsislav K. Valev.

Peer review information *Nature Photonics* thanks Keisuke Goda and the other, anonymous, reviewer(s) for their contribution to the peer review of this work.

Reprints and permissions information is available at www.nature.com/reprints.